ROYAL SOCIETY
OF CHEMISTRY

PAPER

Check for updates

CuO nanoparticles: green combustion synthesis, applications to antioxidant, photocatalytic and sensor studies

Raju Prakruthi[a] and Hemavathi Nagaraju Deepakumari ✩[*ab]

The use of metal oxide nanoparticles for heterogeneous photodegradation is a prominent method for the removal of organic dyes from water resources. Compared to conventional approaches to treat polluted water, it is a more preferable method because of its environmental friendliness, low cost, and no requirement of extreme temperature and pressure. Among all the nanoparticles, CuO is a prominent material. Therefore, this study reports on the biogenic preparation of CuO nanoparticles by adopting a combustion method and *Samanea saman* pod extract as fuel. The synthesized nanoparticles were characterized through X-ray diffraction spectroscopy to confirm the crystallinity of CuO; the surface morphology of the material was studied using scanning electron microscopy (SEM) and X-ray photoelectron spectroscopy (XPS) and the purity of the material was confirmed by energy dispersive X-ray spectroscopy. The degradation efficiency of CuO nanoparticles towards methylene blue dye, a model pollutant present in water resources, was assessed and found to be 97% after 90 minutes of light exposure. The synthesized CuO nanoparticles were also examined for antioxidant and electrochemical sensing studies using cyclic voltammetry. Results showed that CuO nanoparticles function as a strong antioxidant and are a very effective electrochemical sensor.

1 Introduction

Owing to urbanization and industrialization, water resources have been negatively impacted, with wastewater effluents posing a severe threat to aquatic ecosystems and humans. These effluents contain organic dyes and insecticides that block sunlight and reduce dissolved oxygen concentrations in water resources. Degradation of organic dyes poses a major problem due to their complex structure. Many water treatment approaches have been explored, including the use of activated carbon, precipitation, flocculation, electrolysis, oxidation–reduction reactions, and coagulation. However, these methods produce secondary products that cause serious problems for humans and aquatic life. Worldwide, textile industries affect approximately 4 million liters of water daily. To overcome this problem, researchers have turned to nanotechnology to develop a progressive oxidation method for deterioration of organic pollutants.[1] Metal oxide nanoparticles such as ZnO,[2] ZrPO4,[3] ZrO2,[4] BiVO4,[5] and NiO[6] have great potential to combat harmful organic dyes. These nanoparticles utilize the complete solar spectrum in the photocatalytic degradation of organic pollutants, generating active oxygen species such as superoxide, free radicals, and peroxides that degrade electron-rich organic pollutants to non-toxic water and carbon dioxide through the mineralization process.

In the last few decades, eco-friendly methods have been the focus for synthesizing metal oxide nanoparticles owing to their safety to animals, plants, and humans. Bacteria, fungus, plants, and algae can carry out physicochemical processes and adopt distinctive forms because they possess substances that function as stabilizing and reducing agents.[7] CuO nanoparticles have unique properties and versatility. Some industrial applications of CuO include its use as a catalyst in various chemical reactions; in the development of batteries, particularly lithium-ion batteries[8] and supercapacitors[9] for enhancing charge storage capacity; in the production of sensors[10] and transistors;[11] and as antimicrobial agents. It is also used in water treatment to remove heavy metals and organic pollutants;[12] in gas detection; and in monitoring hydrogen, methane and carbon monoxide because of their sensitivity to CuO nanoparticles. CuO nanoparticles are among the most useful metal oxide nanoparticles for treating wastewater because of their larger surface area, superior catalytic activity, and less toxicity.[13] Narrow bandgap and monoclinic structure characterize CuO nanoparticles, which are p-type semiconductors. For the synthesis of nanomaterials, a variety of techniques are employed, including hydrothermal,[14] solvothermal,[15] precipitation,[16] and microwave.[17–19] Using a variety of green extracts, including *Amaranthus dubius*,[20] *Mussaenda frondosa*,[21] *Abutilon indicum*,[22]

[a]*Department of Chemistry, Bharathi College, Bharathinagara, Mandya, 571 422, Karnataka, India*

[b]*Department of Chemistry, Regional Institute of Education (NCERT), Bhubaneswar, 751 022, Odisha, India. E-mail: deepakumari_22@yahoo.com*

Table 1 CuO nanoparticles from different plant materials, different methods of synthesis and applications

Nanoparticle	Plant material	Method of synthesis	Applications	References
CuO	*Amaranthus dubius*	Combustion	Sensing and photocatalytic activities	20
CuO	*Mussaenda frondosa*	Combustion	Photocatalytic and biological investigations	21
CuO	*Abutilon indicum*	Combustion	Antimicrobial, antioxidant and photocatalytic activities	22
ZnO–CuO	*Artemisia abyssinica*	One-pot synthesis	Antioxidant, anticancer and molecular docking studies	23
CuO	*Samanea saman* pod	Combustion	Photodegradation, antioxidant and sensing activity	Present work

and *Artemisia abyssinica*,[23] herein, CuO nanoparticles were synthesized by the combustion process. However, using physical and chemical methods and other conventional methods for the synthesis of nanoparticles, there are many drawbacks including the need for costly chemicals, high temperature, critical pressure and equipment as well as the usage of hazardous substances. Green technology is far superior compared to physical and chemical methods based on many factors, for example, green techniques eliminate the use of many expensive chemicals and generate environment-friendly products, by-products consume less energy[19] and these eco-friendly capping agents stabilize the synthesized nanoparticles. Hence, in the present study, we employed a simple combustion approach using green fuel as a natural ecofriendly reducing agent to produce copper oxide nanoparticles. The ability of the produced nanoparticles to degrade photochemically was assessed. Table 1 compares CuO nanoparticles made from various plant resources, synthesis techniques, and applications.

2 Experimental

2.1 Preparation of green extract

A Soxhlet apparatus was used to extract 10 g of the powdered pods 12 times using 200 mL of double distilled water in order to synthesize copper oxide nanoparticles. The resulting aqueous extract was used as a stabilizing and reducing agent.

2.2 Synthesis of CuO nanoparticles

Making use of the solution combustion method, CuO nanoparticles were produced using *Samanea saman* pod extract as

the fuel and cupric acetate monohydrate ($C_4H_8CuO_2$) as a source. A 50 mL silica crucible was filled with 2.496 g (0.01 M) of cupric acetate monohydrate and aliquots of the extract, labelled C1, C2, and C3, respectively, containing 2 mL, 4 mL and 6 mL. The resulting solution was first heated using an electric burner to produce a semisolid material and the optimum combustion temperature was maintained at about 400 °C during calcination in order to avoid overheating, which can cause defects in the synthesis of nanoparticles. The defects can reduce recombination, improve the charge separation, enhance the light absorption, increase the surface reactivity, and improve the adsorption of reactants and catalytic activity. Excessive defects might compromise the structural stability. The polyphenols in the extract, such as alkaloids, steroids, terpenoids, and flavonoids, acted as reducing agents, capping agents, and surfactants for tailoring the CuO nanoparticles. They prevented the agglomeration and destabilization of CuO nanoparticles and influenced the surface morphology. The phenolic hydroxyl groups and oxygen present in the ester bind with the metal by chelation to form a metal-phenolic hydroxyl complex. Copper oxide nanoparticles are produced when these complexes decompose at higher temperatures (Fig. 1 & 2).

2.3 Characterization of the synthesized CuO nanoparticles

The crystallinity and structure of the CuO nanoparticles were assessed using an X-ray diffractometer (Regakou-Smart Lab) furnished with monochromatic high-intensity Cu-Kα radiation, where λ equals 1.5418 angstroms. The surface composition and elementary oxidation states of Cu in the synthesized nanoparticles were investigated using XPS analysis using an AXIS
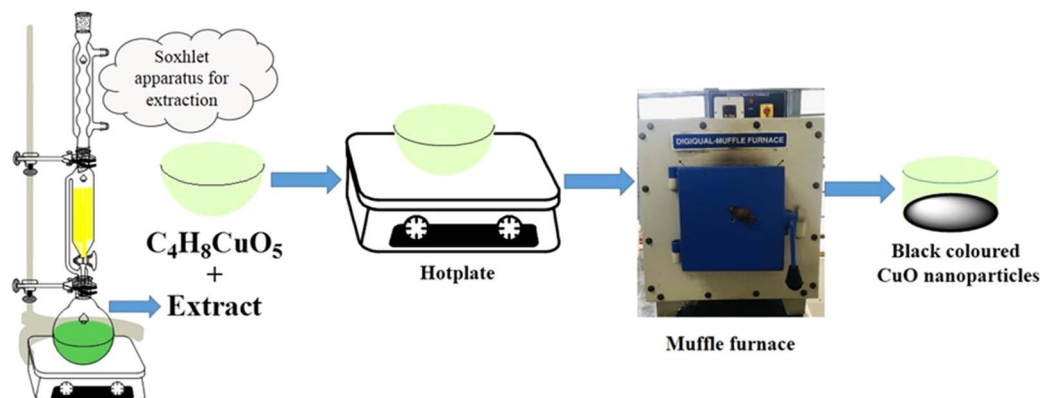
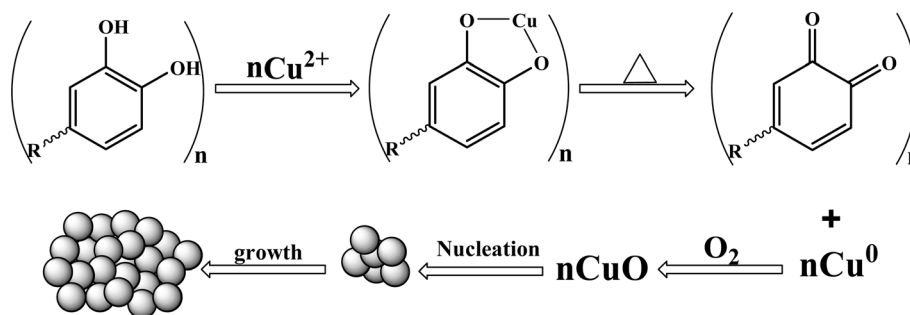**Fig. 1** Schematic representation of CuO nanoparticles.

Fig. 2 The plausible mechanism underlying the formation of CuO nanoparticles by *Samanea saman* pod extract fuel.

ULTRA from AXIS 165, integrated with a Kratos patented magnetic immersion lens, charge neutralization system and spherical mirror analyzer. Using a TESCAN Vega 3LMV instrument, SEM was used to notify the material's surface morphology. The purity and elemental conformation were ascertained by means of energy-dispersive X-ray diffraction analysis coupled with SEM.

2.4 Photocatalytic activity

An annular photoreactor (model HAVR-123, make HEBER Scientific, Chennai, India) with safety wood covered with an anti-reflective substance was used to study the photocatalytic activity of methylene blue dye. The reactor can hold eight cylindrical tubes with a 100 mL capacity for the reaction mixture. The tubes were placed four cm away from the light source, which was a 250 W UV light placed in the middle of a water-cooled jacket and surrounded by eight cooling fans in the wood. Initially, 50 mg of copper oxide was dissolved in 5 ppm MB dye, and the solution was mixed and transferred to a cylindrical tube. In order to achieve absorption–desorption equilibrium, the solution was maintained in a dark environment with aeration for thirty minutes. Then, the tubes were irradiated with visible light, and after every 20 minutes, a 2 mL

sample was withdrawn and centrifuged using a microcentrifuge to separate copper oxide nanoparticles from the solution. The absorbance was then determined by analyzing the solution at 663 nm using an Agilent Cary 60 UV-visible spectrophotometer. Many factors, including pH variation, catalyst load variation, and dye concentration, were taken into account when conducting the experiment. Ultimately, eqn (1) was utilized to compute the % degradation.

$$\text{Percentage of degradation} = \frac{C_i - C_f}{C_i} \times 100 \qquad (1)$$

where C_i is the initial concentration and C_f is the concentration of the dye after certain amounts of time.

2.5 Electrochemical properties

The synthesized CuO nanoparticles were examined for electrochemical sensor properties using cyclic voltammetry.

3 Results and discussion

3.1 X-ray Diffraction studies

The crystalline purity and crystal structure of biogenically synthesized CuO nanoparticles were ascertained by analyzing
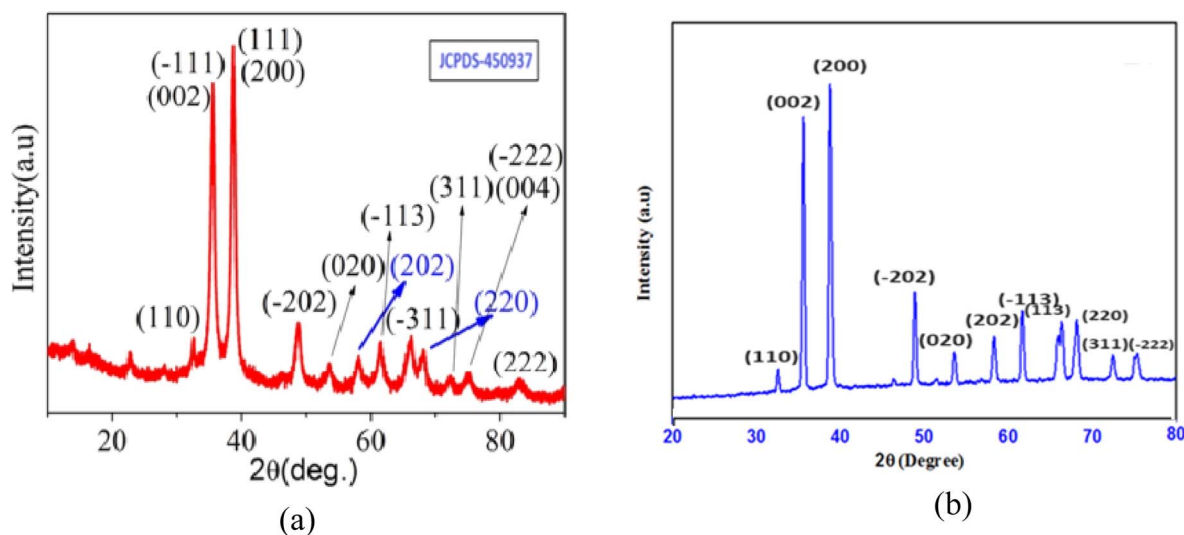

Fig. 3 (a) Standard XRD spectra of CuO nanoparticles and (b) XRD spectra of the synthesized CuO nanoparticles.
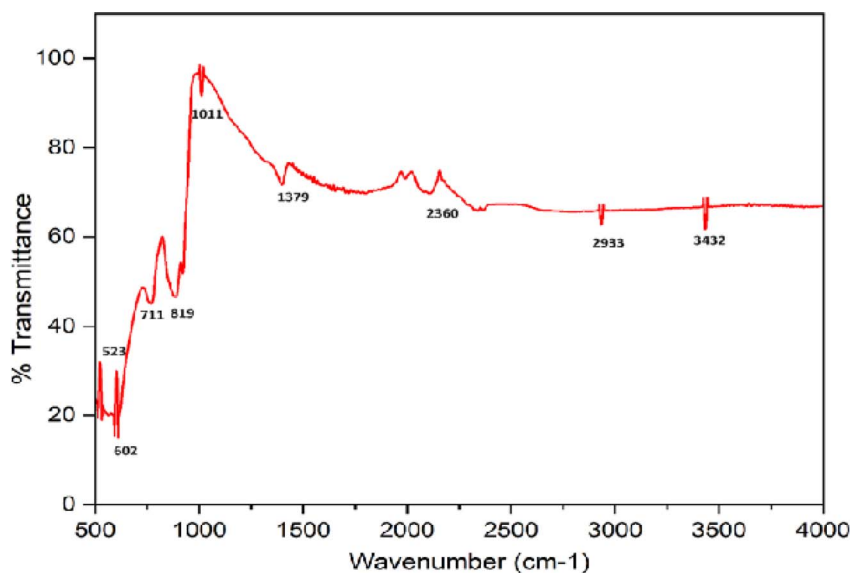
Fig. 4 FTIR spectrum of the synthesized CuO nanoparticles.

their XRD patterns, which are displayed in Fig. 3a and b. A set of diffraction patterns at θ values of 32.4°, 35.4°, 38.7°, 48.7°, 58.5°, 61.8°, 65.7°, and 75.2° was found in the analysis. These patterns were assigned to the (110), (002), (200), (202), (202), (113), (311), and (004) planes of monoclinic CuO, in that order. All the obtained planes were in agreement with the International Center of Diffraction Data Card, JCPDS No. 450937.[24–26] The lattice parameters were $a = 4.84$ Å, $b = 3.425$ Å, $c = 5.129$ Å, and $\beta = 99.5°$. Based on the values of ($2\theta = 35.4°$, 38.7°, 48.7°), the crystallite size was determined to be 12 nm using the Debye–Scherrer formula that is discussed below (eqn (2)). The XRD analysis revealed no impurity peaks, indicating a high degree of purity in the crystalline phase.

$$D = \frac{0.89\lambda}{\beta \cos\theta} \qquad (2)$$

where, D = crystallite size, λ = X-ray wavelength, β = full width at the half maximum, θ = is the diffraction angle.

3.2 Fourier transmission infrared (FTIR) studies

The FTIR spectrum of CuO NPs produced *via* the green approach is shown in Fig. 4. The stretching vibration of the Cu–O bond in monoclinic CuO was responsible for the infrared bands at 603 cm^{-1}.[27] CuO's M–O stretching vibrations are responsible for the other two peaks, which are located at 819 and 711 cm^{-1}.[28] The bending and stretching vibrations of water molecules and the surface hydroxyl groups adsorbed on the surface of CuO NPs may be the cause of the absorption peaks that arise at 1379 and 3432 cm^{-1}.[29] The creation of CuO from the green synthesis is confirmed by the presence of significant infrared bands at about 400–600 cm^{-1}.

3.3 X-ray photoelectron spectroscopy (XPS) analysis

The XPS spectra of CuO nanoparticles is displayed in Fig. 5a and b. The resultant spectrum showed a calculated binding energy (BE) for the C 1s electron at 284.3 eV. Cu 2p$_{3/2}$ and Cu 2p$_{1/2}$ are
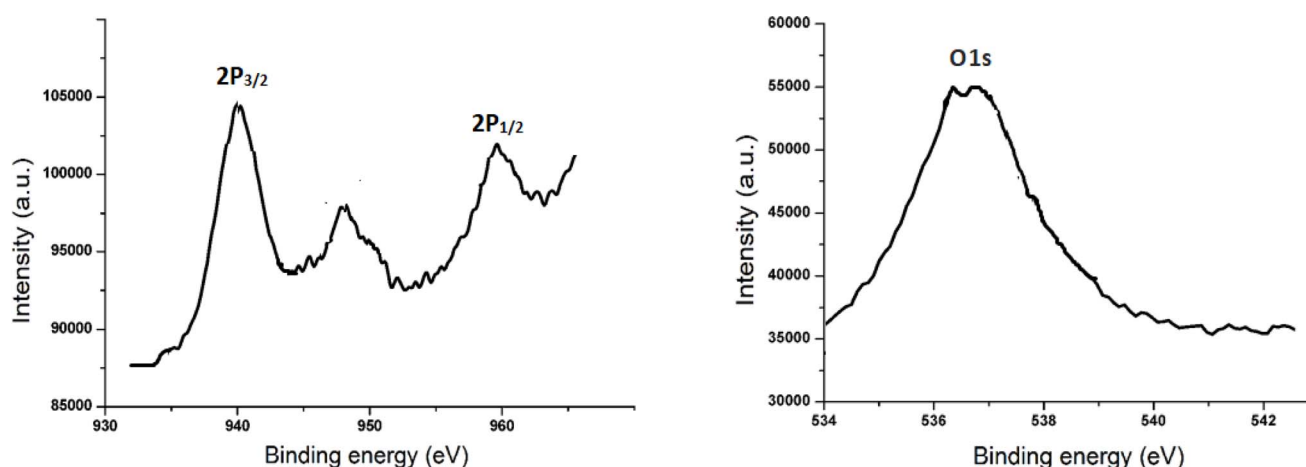

Fig. 5 XPS spectra of CuO nanoparticles, (a) Cu 2p and (b) O 1s.

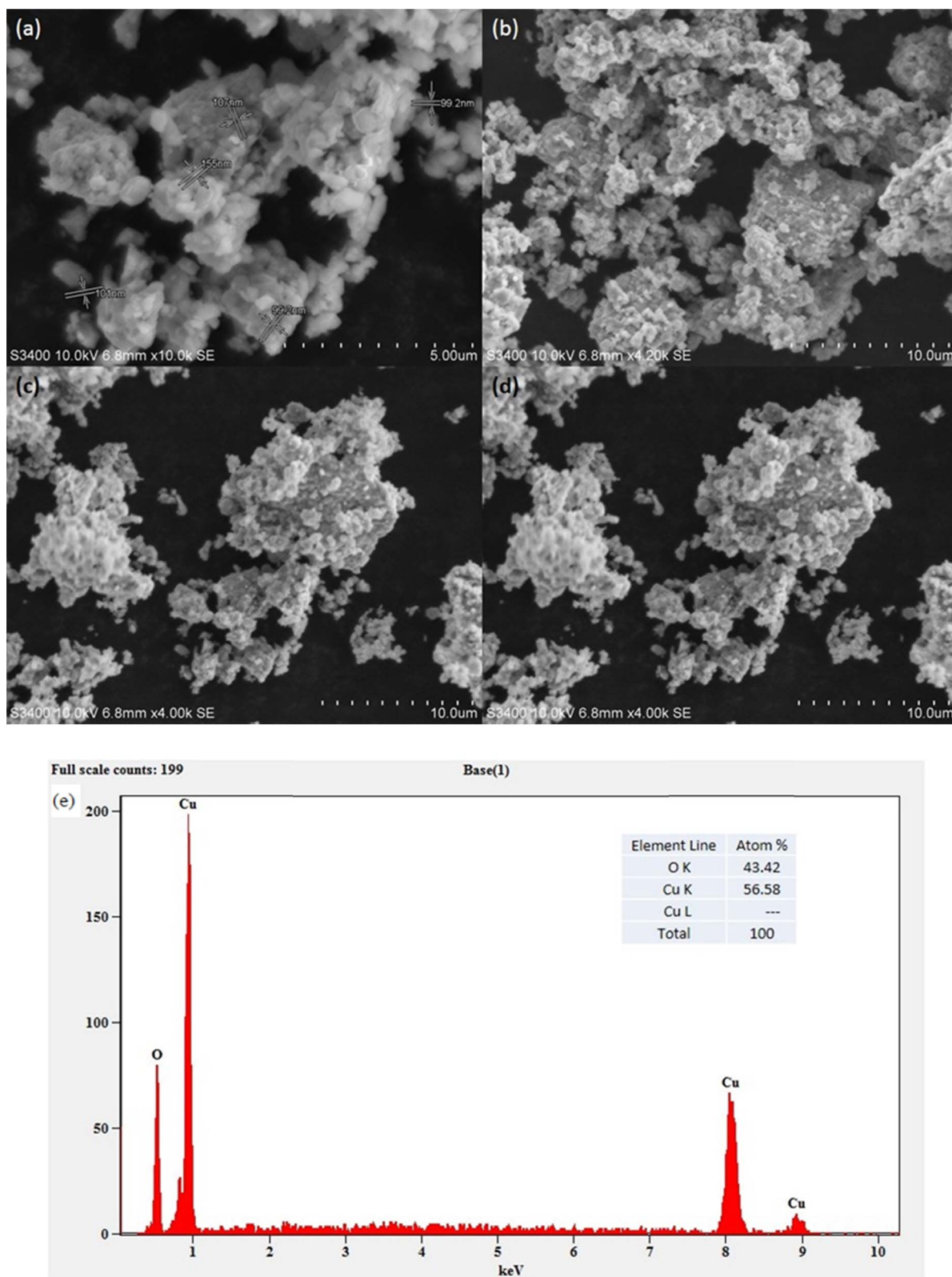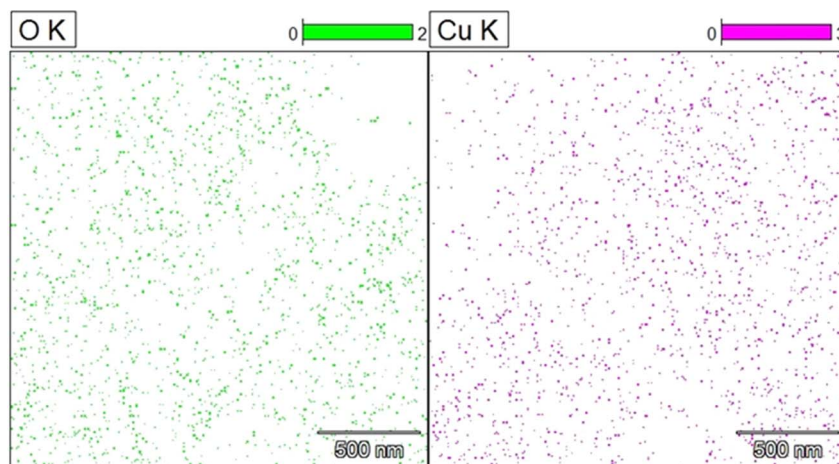**Fig. 6** SEM images (a– d) and (e) EDS spectrum of the synthesized CuO nanoparticles.

Fig. 7   Elemental mapping of the synthesized CuO nanoparticles.
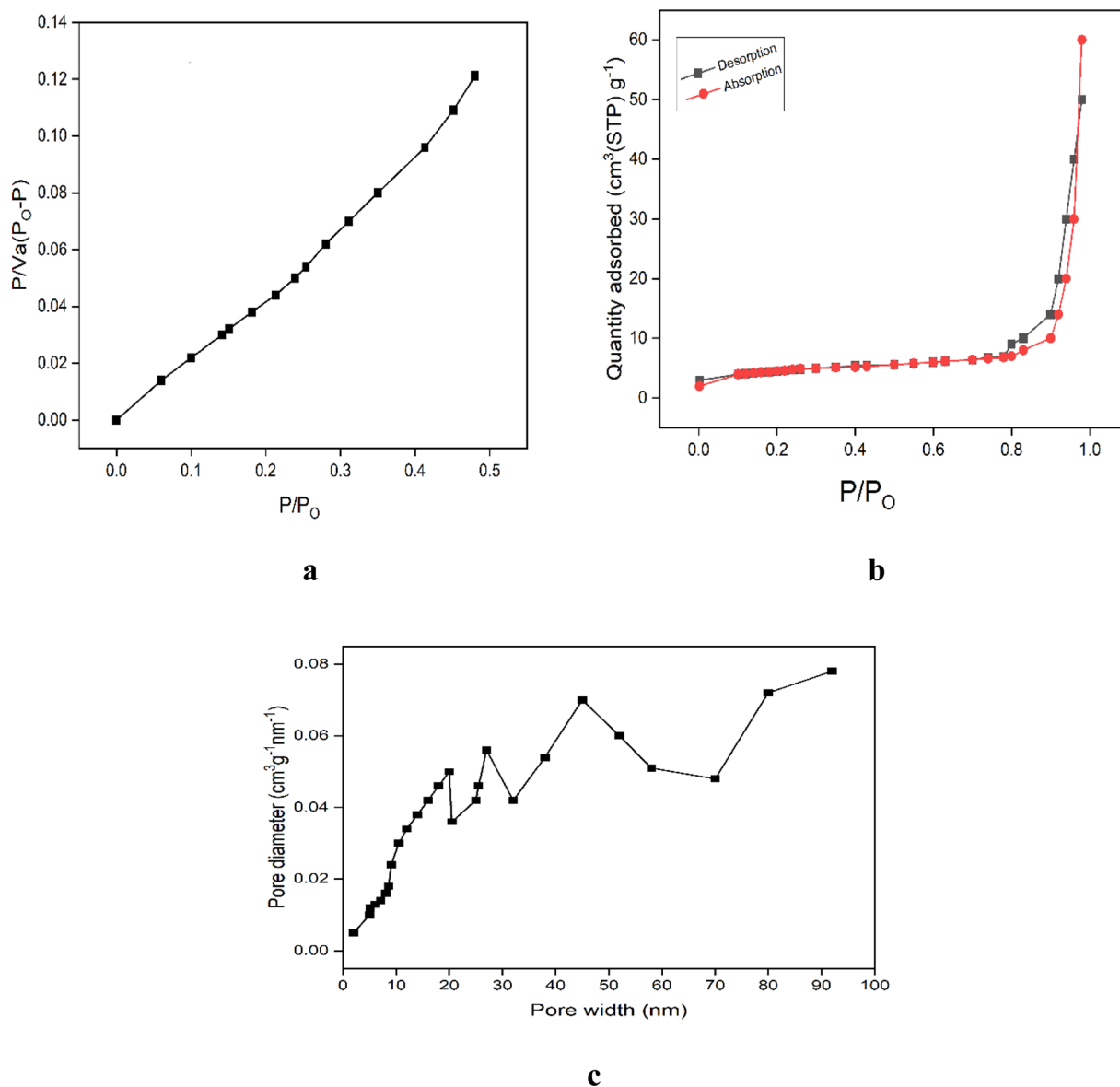

a

b

c

Fig. 8   (a) BET plot of CuO NPs, (b) nitrogen desorption–adsorption isotherm, and (c) BJH plot of CuO NPs.

represented by the XPS BE at 941.3 and 957.4 eV, respectively. The O 1s of CuO nanoparticles is correlated with the BE at 535 eV. The reported data provides substantial support for the outcome.[30,31] There are no contaminants in the sample, according to the XPS determination.

3.4 Morphological and elemental mapping

Using scanning electron microscopy (SEM), the surface appearance of the synthesized CuO nanoparticles was characterized. The spherical nature of the CuO nanoparticles was clear from the SEM images (Fig. 6a–d). CuO nanoparticles were found to contain 56.6% copper and 43.4% oxygen, according to the energy dispersive X-ray spectrum (Fig. 6e). The synthesis was carried out using a green extract, but other elements were not present. This could be a result of the synthesized materials that were calcined for four hours at 400 °C. Elemental mapping showed an even distribution of copper and oxygen (Fig. 7).

3.5 Surface morphology

Surface morphology gives information about the surface area, pore size and pore volume of the synthesized nanoparticles using BET analysis, nitrogen desorption–adsorption isotherm and BJH study, respectively. N_2 adsorption was used to determine the BET surface area using a surface analysis device (Beishide, 3H-2000PSI, China). Fig. 8a shows the BET surface area with correlation coefficient $R^2 = 0.9988$. The nitrogen

desorption/adsorption isotherms are depicted in Fig. 8b, while the Barret–Joyner–Halenda (BJH) pore size distributions that correspond to CuO NPs are displayed in Fig. 8c. The pore volume and pore size of green synthesized CuO nanoparticles were found to be 0.997 cm^3 g^{-1} and 9.12 nm, respectively, by BJH evaluation. The pore shape in the synthesized sample is represented by the type IV nitrogen isotherm, which has a surface area of 21.54 m^2 g^{-1} and a hysteresis loop.

4 Applications

4.1 Degradation efficiency of CuO nanoparticles

The photocatalytic properties of the synthesized CuO nanoparticles[32–34] were studied using methylene blue organic dye under a visible light source. In our work, we prepared CuO nanoparticles using combustion synthesis with *Samanea saman* pod extract as a fuel and observed good catalytic activity at different parameters. The higher surface area and adsorption capacity of the nanoparticles were responsible for the improved photocatalytic activity. In order to achieve adsorption–desorption equilibrium, the reaction mixture was first maintained in a dark environment, and no degradation activity was seen. However, when the reaction mixture was exposed to light irradiation, hydroxyl radicals, superoxides, and peroxides were produced in the aqueous solution containing the photocatalyst. The photo-generated hydroxyl radicals then reacted with methylene blue dye, leading to oxidation, cleavage of rings, and changes in the conjugation and structure of methylene blue. The experiment was performed for all the materials (C1, C2, and C3), and C3 showed a higher percentage of degradation compared to the others due to its larger surface area shown in Fig. 9. A larger surface area provides more active sites for the photocatalytic reaction, improves light absorption, allows for the better adsorption of reactants onto the photocatalyst surface and enhances the higher photocatalytic activity. From Fig. 8, we observed that C3 material shows maximum photocatalytic activity due to the larger surface area. The degradation efficiency of the synthesized CuO nanoparticles with other metal nanoparticles are shown in Tables 2 and 3, respectively. The mechanism of photocatalytic activity shown in Fig. 10 and the probable reaction mechanism is written below.
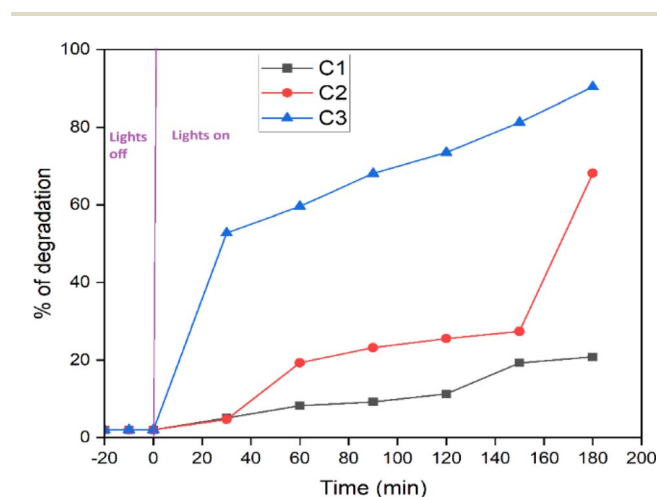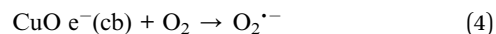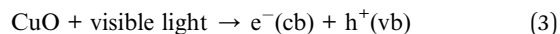
$$CuO + visible\ light \rightarrow e^-(cb) + h^+(vb) \quad (3)$$

$$CuO\ e^-(cb) + O_2 \rightarrow O_2^{\bullet-} \quad (4)$$

Fig. 9 Photodegradation activity of C1, C2 and C3 materials of CuO nanoparticles.
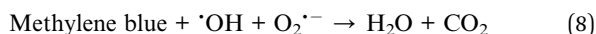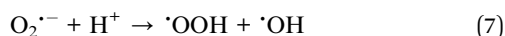
Table 2 Degradation efficiency of CuO nanoparticles

Nanomaterials	Light source	Degradation time	Degradation efficiency	References
CuO NPs	Sun light	120 min	63%	35
CuO NPs	Sun light	150 min	84%	36
CuO NPs	UV light	7 hours	98%	37
CuO NPs	UV light	120 min	96.93%	38
	Sunlight	120 min	80%	
CuO NPs	Visible light	120 min	90%	Present work

Table 3 Comparison of the degradation efficiency of different metal oxide nanoparticles

Metal oxide	Light source	Degradation time	Degradation efficiency in%	References
Fe_2O_3	UV light	56 min	95.08	39
CoO	Solar light	50 min	78.45	40
ZnO	UV light	1 hour	94	41
CeO_2	UV light	120 min	93	42
NiO	Visible light	50 min	84	43
Ag/Ag_2O	UV light	50 min	84.5	44
PbO	UV light	150 min	90	45
$Sr_6(Ga_{12}O_{24})\cdot BiO_3$	UV light	150 min	93	46
CuO NPs	Visible light	120 min	90	Present work

$$CuO\,(h^+) + H_2O \rightarrow OH^\cdot + H^+ \quad (5)$$

$$OH^- + h^+(vb) \rightarrow OH^\cdot \quad (6)$$

$$O_2^{\cdot-} + H^+ \rightarrow {}^\cdot OOH + {}^\cdot OH \quad (7)$$

$$Methylene\ blue + {}^\cdot OH + O_2^{\cdot-} \rightarrow H_2O + CO_2 \quad (8)$$

4.1.1 The effect of photocatalyst dosage. Fig. 11 illustrates the results of a study conducted on CuO (C3) nanoparticles at ten, twenty, thirty, and forty milligram doses. At a dosage of 30 mg, the removal efficiency was 92%; at 40 mg, the degradation efficiency marginally dropped to 70%. The great light absorption of CuO nanoparticles, which increases the production of photogenerated holes and electrons, is the cause of this effectiveness. These charge carriers generate hydroxyl and superoxide radicals when they combine with water and dissolved oxygen. But when the dosage rises, light transmittance falls, which affects light consumption and lowers the
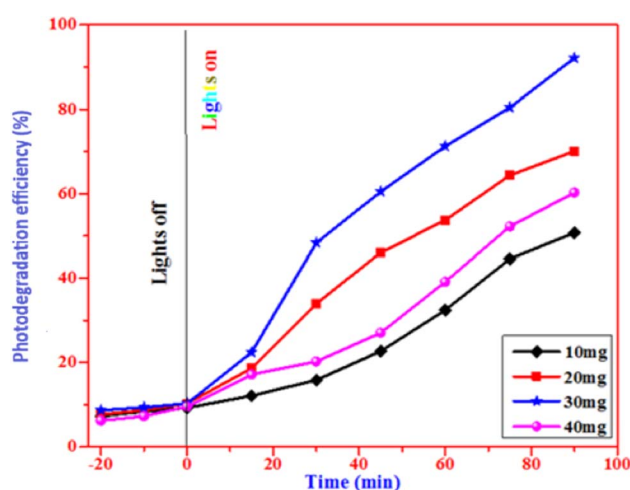

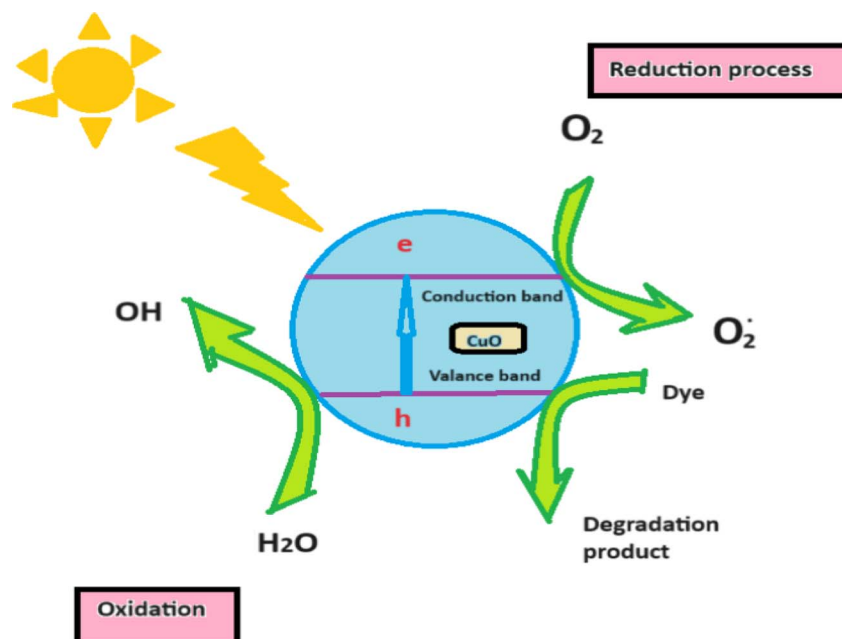**Fig. 11** Photodegradation efficiency of CuO nanoparticles at different loads.

Fig. 10 Diagrammatic representation for the mechanism of the photocatalytic activity of the synthesized CuO nanoparticles.

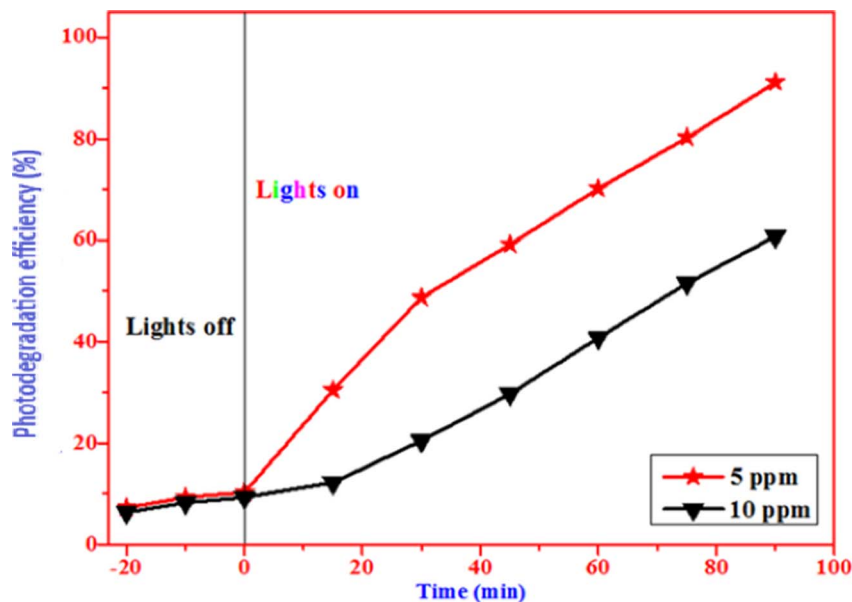© 2024 The Author(s). Published by the Royal Society of Chemistry

Fig. 12 Photocatalytic activity of CuO nanoparticles at different dye concentrations.

photodegradation efficiency. Moreover, removal efficiency is the result of nanoparticle aggregation due to an additional increase in the dose.

4.1.2 Optimization of dye concentration. Fig. 12 illustrates the optimization of dye concentration for the enhanced photocatalytic degradation of methylene blue. The concentration of the dye was varied from 5 ppm to 10 ppm, while the concentration of CuO nanoparticles was kept constant at 30 mg. As shown in the figure, the photodegradation activity gradually decreases from 90% to 60% as the dye concentration increases from 5 ppm to 10 ppm. The highest effective degradation was observed at 5 ppm, with approximately 91% efficiency. It may be observed from the data that there is a decrease in dye degradation because larger molecules of dye adsorb on the catalyst's

surface. The drop in the degradation efficiency could perhaps be attributed to an increase in dye concentration and increased light penetration.

4.1.3 The effect of pH on the photodegradation efficiency. We investigated the photodegradation efficiency of CuO nanoparticles by varying the solution's pH from 2 to 11. Fig. 13 showed that when the pH of the solution increases, the efficiency decreases. Because CuO is positively charged in basic pH levels above 11, while methylene blue is negatively charged in acidic media, which accounts for the reduction in efficiency. As the pH increases, OH^- ions adsorb on the surface of the catalyst, and the catalyst becomes negatively charged, leading to repulsion between negatively charged methylene blue and CuO nanoparticles. Additionally, there is an increase in electron–
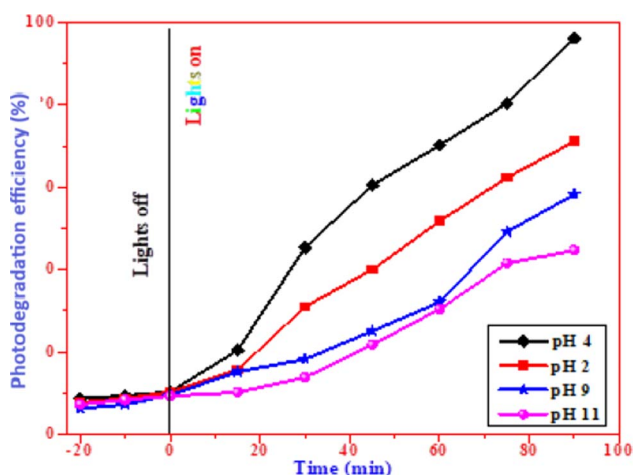

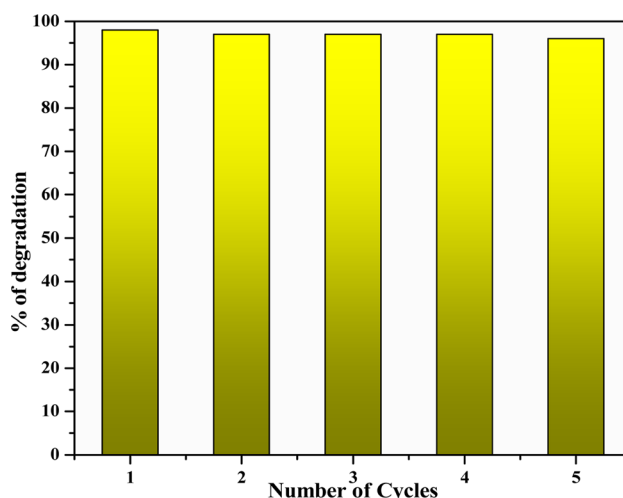**Fig. 13** Photocatalytic activity of CuO nanoparticles at different pH values.

Fig. 14 Recyclability of CuO nanoparticles.

hole recombination, which decreases the degradation efficiency. Since positively charged CuO nanoparticles and negatively charged methylene blue dye are attracted to one another, more oxidation–reduction reactions occur, making pH 4–5 the ideal pH range to enhance the degradation efficiency.

4.2 Reusability of the catalyst

The stability of the photocatalyst was checked through recycled trials using methylene blue organic dye. The experiment employed 100 cm^3 of 5 ppm methylene blue dye and 100 mg of CuO photocatalyst in total. The photocatalyst was removed from the cycle, cleaned with deionized water, and then reused. For the first five cycles, the photodegradation efficiency of CuO nanoparticles was basically unaffected. Fig. 14 illustrates the 2% drop in efficiency that occurred on the sixth cycle. However, the stable structure of CuO nanoparticles was primarily responsible for the good efficiency.

4.3 Treatment of waste water sample by the synthesized CuO nanoparticles

The waste water sample were was from Kachanayakanahalli lake, Bengaluru, Karnataka. The synthesized nanoparticles were added to 100 mL of the water sample, kept under visible light and at every 30 min interval, the samples were collected and tested. Fig. 15 shows that about 93% of dye degradation takes place in 180 min.

4.4 Photoluminescence study by the detection of hydroxyl radicals

This study suggests that the reactive hydroxyl ions are responsible for the degradation of the organic dye and the stability of hydroxyl species present in the green fuel formed during the photodegradation process. Herein, we prepared 0.001 M coumarin solution for 10 mg catalyst. The solution was kept under photodegradation for 30 minutes. A photoluminescence spectrophotometer was used to measure the sample at 10 minutes intervals. The increase in the amount of hydroxyl
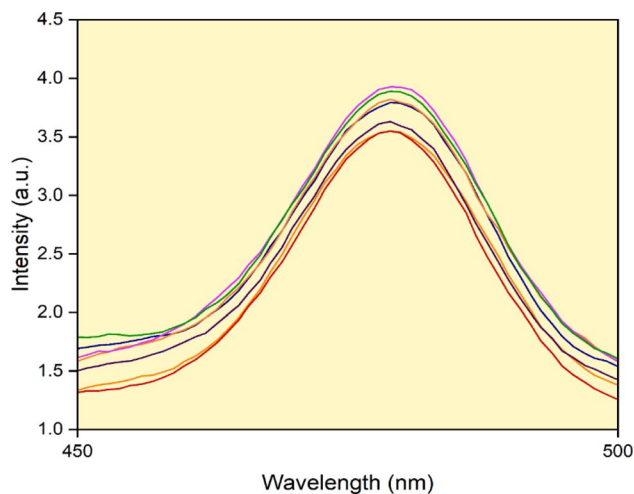

Fig. 16 PL spectrum for the detection of OH radicals.

radicals, as illustrated in Fig. 16, causes the intensity of the peak to increase as the irradiation time increases. By this process, we conclude that reactive oxygen species are very significant for photodegradation.

5 Antioxidant property

Biochemical processes in living things are significantly affected by antioxidants. Active oxygen species and free radicals were produced under normal physiological circumstances. Tissue damage results from biomolecules oxidation when they are harmful to cells. It is necessary to remove this cell from the system since it expires and causes human health syndromes like as cancer, aging, arthritis, and neurological disease. In the current investigation, the DPPH radical is used for scavenging studies. The mechanism of the antioxidant activity of CuO nanoparticles is shown in Fig. 17. The electrostatic affinity between charged bioactive molecules and CuO-NPs may account for the highest antioxidant competency of CuO-NPs against the DPPH radical. The IC$_{50}$ values for L-CuO NP (1570 μg mL^{-1}) and S–CuO NP (1536 μg mL^{-1}) were found, while the IC$_{50}$ value for C–CuO NP (2044 μg mL^{-1}) was the highest, as shown in Fig. 18.

6 Electrochemical properties

The electrochemical sensor comprises of three electrodes, namely, working/sensing, reference and counter electrodes,
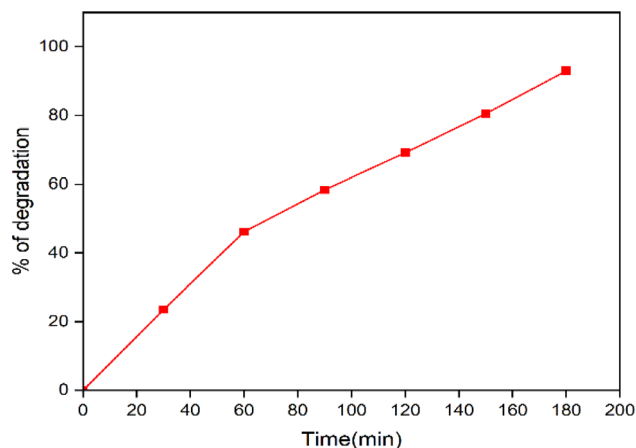

Fig. 15 Photocatalytic dye degradation efficiency of CuO nanoparticles in the water sample.
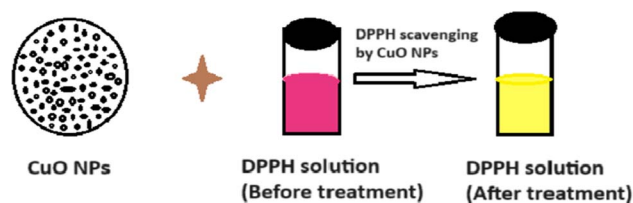

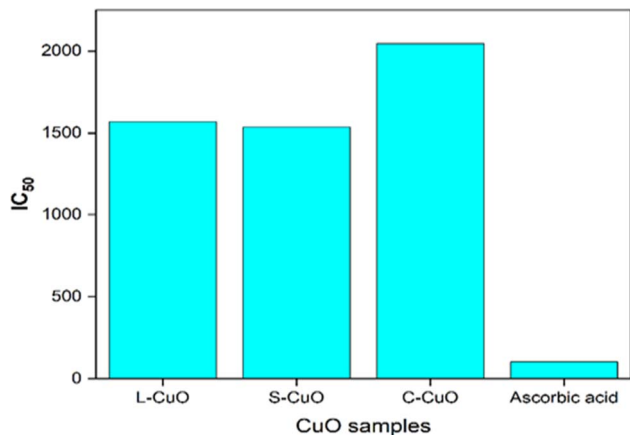Fig. 17 Mechanism of antioxidant activity of CuO NPs.
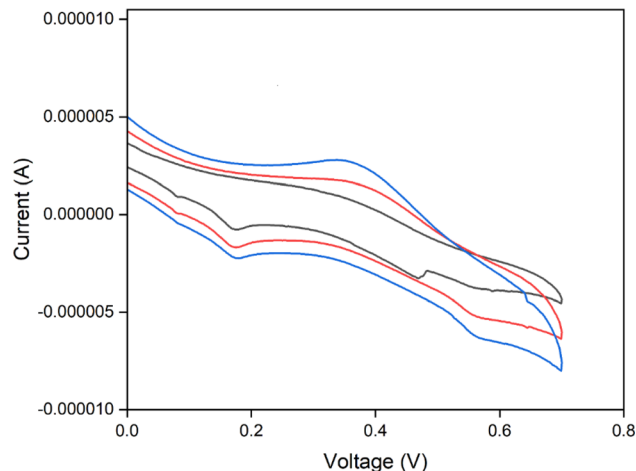
Fig. 18 Antioxidant activity of CuO-NPs.

Fig. 19 Mechanism of electrochemical sensing of the synthesized CuO NPs.

Fig. 20 Cyclic voltammetry curve for CuO nanoparticles.

which is connected to complete the circuit for current flow. Numerous electrochemical methods are available for biosensors, such as impedimetric (impedance at the electrode surface), potentiometric (measures change in potential), and amperometric (measures current produced because of the sample's redox reaction).[47] Fig. 19 shows the mechanism of electrochemical sensing of the synthesized CuO nanoparticles.

Fig. 20 displays the cyclic voltammetry plot of the scan rates of CuO nanoparticles. These curves indicate the redox peaks in the corresponding anodic and cathodic scans. The cathodic and anodic peaks in the scan illustrate the pseudo-capacitive behaviour of CuO. A number of electrochemical tests was performed with 0.1 M HCl, lead nitrate, and ascorbic acid in order to characterize the synthesized CuO nanoparticles based on the sensor. Cyclic voltammetry (CV) was used in the sensor studies and the curves are shown in Fig. 18. In 0.1 M HCl, a three-standard electrode system was used for CV analysis.[48,49] This analysis was carried out in the absence of ascorbic acid or lead nitrate using a scan rate ranging from 10 mV s^{-1} to 50 mV s^{-1}. The reduction peaks were found to be at potentials of -0.1 V and 0.3 V, whereas the oxidation peaks were observed at

potentials of -0.15 V and 0.18 V. In a 0.1 M HCl solution, the specific capacitance values drop as the scan rate increases from 10 mV s^{-1} to 50 mV s^{-1}. As the scan rate increases from 10 mV s^{-1} to 50 mV s^{-1}, the specific capacitance values decrease in the 0.1 M HCl solution. Hence, the synthesized CuO exhibits electrochemical behavior.

7 Conclusion

In summary, CuO NPs were synthesized utilizing a safe, green extract without producing toxic substances that could be harmful to the environment using *Samanea saman* pod extract as a reducing agent. The properties of the CuO nanoparticles were characterized using spectroscopic techniques, including X-ray diffraction, scanning electron microscopy, X-ray photoelectron spectroscopy and energy dispersive X-ray spectroscopy. Using methylene blue dye as a model pollutant found in water resources, the degradation efficiency of CuO nanoparticles was assessed to be 97% after 90 minutes of light exposure. The findings of the present study showed that CuO nanoparticles function as a potential candidate for the photocatalytic degradation of organic dyes and act as a strong antioxidant and a very effective sensor material.

Data availability

The data obtained during this work will be provided by the corresponding author upon request.

Author contributions

PR and HND prepared the materials, collected the data, and did the analysis. PR wrote the initial draft of the paper, while the HND provided feedback on earlier drafts. The design and conception of the study were contributions from both the authors and the final manuscript was read and approved by both the authors.

Conflicts of interest

Acknowledgements

References

1 G. N. Kokila, C. Mallikarjunaswamy and V. L. Ranganatha, *Inorg. Nano-Met. Chem.*, 2021, **12**, 90–97.

2 C. Mallikarjunaswamy, V. L. Ranganatha, R. Ramu and G. Nagaraju, *J. Mater. Sci.: Mater. Electron.*, 2018, **31**, 1–18.

3 V. Sankar, S. Nishkala, K. Gaber, E. E. Saikh and M. Wabaidur, *Appl. Nanosci.*, 2022, **13**, 6093–6103.

4 H. N. Deepakumari, V. L. Ranganatha, G. Nagaraju, R. Prakruthi and C. Mallikarjunaswamy, *Mater. Today: Proc.*, 2022, **62**, 5169–5173.

5 R. Hajipour and H. Karimi, *Mater. Lett.*, 2014, **116**, 356–358.

6 V. L. Ranganatha, G. Nagaraju, J. S. Vidya, H. N. Deepakumari and D. M. Gurudutt, *Mater. Today: Proc.*, 2022, **62**, 5067–5070.

7 S. Pramila, G. Nagaraju, C. Mallikarjunaswamy, K. C. Latha, S. Chandan, R. Ramu, V. Rashmi and V. L. Ranganatha, *Anal. Chem. Lett.*, 2020, **10**, 298–306.

8 C. Wang, D. Higgins, F. Wang, D. Li, R. Liu, G. Xia, N. Li, Q. Li, H. Xu and G. Wu, *Nano Energy*, 2014, **9**, 334–344.

9 P. D. Deepak, G. S. Girish, D. L. Chandrakant and H. Rudolf, *Mater. Res. Bull.*, 2013, **48**, 923–928.

10 S. Reddy, B. E. Kumara swamy and H. Jayadevappa, *Electrochim. Acta*, 2012, **61**, 78–86.

11 C. Florica, A. Costas, A. G. Boni, R. Negrea, L. Ion, N. Predda, L. Pintillie and I. Enculescu, *Appl. Phys. Lett.*, 2015, **106**, 223501.

12 M. Ramesh, *Water Pract. Technol.*, 2021, **16**, 1078–1090.

13 J. S. Souza, F. T. H. Hirata and P. Corio, *J. Nanopart. Res.*, 2019, **21**, 1–9.

14 S. Pramila, V. L. Ranganatha, G. Nagaraju and C. Mallikarjunaswamy, *Inorg. Nano-Met. Chem.*, 2022, **53**, 1–12.

15 N. C. Z. Moghadam, S. A. Jasim, F. Ameen, D. H. Alotaibi, M. A. L. Nobre, H. Sellami and M. Khatami, *Bioprocess Biosyst. Eng.*, 2022, **45**, 1201–1210.

16 M. Chandrasekar, M. Subash, S. Logambal, G. Udhayakumar, R. Uthrakumar, C. Inmozhi, W. A. Al-Onazi, A. M. Al-Mohaimeed, T. W. Chen and K. J. Kanimozhi, *J. King Saud Univ.*, 2022, **34**, 101831.

17 L. Marinescu, D. Ficai, A. Ficai, O. Oprea, A. I. Nicoara, B. S. Vasile, L. Boanta, A. Marin, E. Andronescu and A. M. Holban, *Int. J. Mol. Sci.*, 2022, **23**, 5982–5989.

18 R. Vijayakumar, Y. Sivaraman, K. M. Pavagada Siddappa and J. P. R. Dandu, *Int. J. Polym. Anal. Charact.*, 2022, **27**, 99–110.

19 M. Sundararajan, A. Subramani, M. Ubaidullah, S. F. Shaikh, B. Pandit, S. K. Jesudoss, M. Kamalakannan, S. Yuvaraj, P. S. Subudhi and C. S. Dash, *J. Cluster Sci.*, 2022, **33**, 1–10.

20 J. Akter, K. P. Sapkota, M. A. Hanif, M. A. Islam, H. G. Abbas and J. R. Hahn, *Mater. Sci. Semicond. Process.*, 2021, **123**, 105570.

21 P. Yusuf Ansari, R. M. Muthukrishnan, I. Khan, C. Vedhi, K. Sakthipandi and S. M. Abdul Kader, *Chem. Phys.*, 2023, **7**, 100374.

22 B. Malaikozhundan, V. N. Lakshmi and R. Krishnamoorthi, *Mater. Today Commun.*, 2022, **33**, 104348.

23 P. C. Udayabhanu, M. A. Nethravathi, D. Pavankumar, K. Suresh, K. Lingaraju, H. Rajanaika, H. Nagabhushana and S. C. Sharma, *Mater. Sci. Semicond.*, 2015, **33**, 81–88.

24 F. Yang, J. Guo, M. Liu, S. Yu, N. Yan, J. Li and Z. Guo, *J. Mater. Chem. A*, 2015, **3**, 20419–20828.

25 D. W. Kim, K. Y. Rhee and S. J. Park, *J. Alloys Compd.*, 2012, **530**, 6–10.

26 W. T. Yao, S. H. Yu, Y. Zhou, J. Jiang, Q. S. Wu, L. Zhang and J. Jiang, *J. Phys. Chem. B*, 2005, **109**, 14011–14016.

27 X. Zhu, K. Pathakoti and H. M. Hwang, *Green Synth., Charact. Appl. Nanopart.*, 2019, **10**, 223–263.

28 V. T. V. Padil and M. Cernik, *Int. J. Nanomed.*, 2013, **8**, 889–898.

29 C. Tamuly, I. Saikia, M. Hazarika and M. R. Das, *RSC Adv.*, 2014, **4**, 53229.

30 C. H. Yoo and T. W. Kim, *J. Ceram. Process. Res.*, 2011, **12**, 606.

31 Y. Xu, D. Chen, X. Jiao and K. Xue, *Mater. Res. Bull.*, 2007, **42**, 1723–1731.

32 H. R. Chitme, R. Chandra and S. Kaushik, *Phytother. Res.*, 2005, **19**, 454–456.

33 D. J. Manasa, K. R. Chandrashekar, D. J. Madhu Kumar, M. Niranjana and K. M. Navada, *Arabian J. Chem.*, 2021, **6**, 103184.

34 S. A. Akintelu, A. S. Folorunso, F. A. Folorunso and A. K. Oyebamiji, *Heliyon*, 2020, **6**, 04508.

35 L. Faheem, S. Sammia, A. K. Shakeel, A. Waqar and J. Sabah, *Trop. J. Pharm. Res.*, 2017, **16**, 743–753.

36 O. A. Temesgen, E. A. Zereffa, H. C. Ananda Murthy, T. B. Demissie, O. Pardeshi, L. S. Avhad and G. Suresh, *ACS Omega*, 2023, **44**, 41039–41053.

37 K. B. Kusuma, M. Manju, C. R. Ravikumar, V. G. Dileepkumar, A. Naveen Kumar and M. S. Santosh, *Inorg. Nano-Met. Chem.*, 2022, **52**, 295–301.

38 H. C. Ananda Murthy and K. Gurushantha, *J. Nanomater.*, 2022, **13**, 3256611.

39 K. M. Mamatha, V. Srinivasa Murth, C. R. Ravikumar, H. C. Ananda Murthy, M. W. Alam, V. Vinutha and A. A. Jahagirdar, *Inorg. Nano-Met. Chem.*, 2022, **52**, 295–301.

40 N. N. Bibi, S. Atab, M. Sultanb, A. Ali, A. Abbas, K. Jilani, S. Kamal, F. M. Sarimf, M. I. Khang, F. Jalal and M. Iqbal, *J. Mater. Res. Technol.*, 2019, **8**, 6115–6124.

41 Bibi, N. Nazar, H. Nawaz, S. Nouren, Y. Safa, K. Jilani, M. Sultan, S. Ata, F. Rehman and M. Abbas, *Adv. Powder Technol.*, 2017, **28**, 2035–2043.

42 R. Raghunathan, S. Veluswamy, J. l. Nallasamy, M. Shanmugamoorthy, J. Johny, S. Veerasamy, D. Gopalakrishnan, M. Nithyanandham, D. Balamoorthy and P. Veluswamy, *J. Nanomater.*, 2022, **1**, 3863184.

43 D. M. Druzian, L. R. Oviedo, S. N. Loureiro, R. D. Wouters, B. S. Vizzotto, E. D. O. Pino, N. J. S. D. Vanconcellos, Y. P. M. Ruiz, A. Galembeck, G. Pavoski, D. C, R. Espinosa, C. D. Santos and W. L. D. Silva, *J. Photochem. Photobiol., A*, 2023, **442**, 114773.

44 J. Christy, S. Sagadevan and L. C. Nehru, *Optik*, 2021, **237**, 166731.

45 M. A. Awad, A. A. Hendi, K. M. Ortashi, B. Alzahrani, D. Soliman, A. Alanazi, W. Alenazi, R. M. Taha, R. Ramadan, M. E. Tohamy, N. Almasoud and T. S. Alomar, *Sens. Actuators, A*, 2021, **323**, 112670.

46 M. R. B. Omidtorshiz, M. Momennezhad, Z. Sabouri and M. Darroudi, *Inorg. Chem. Commun.*, 2023, **158**, 111575.

47 L. Huai, L. N. Zhang, B. B. Zhang, G. Jia, W. D. Yao, W. D. Liu and R. L. Tang, *J. Solid State Chem.*, 2022, **316**, 123634.

48 D. A. Raghupathy, G. Ramgopal and C. R. Ravikumar, *Sens. Int.*, 2022, **3**, 100204.

49 B. Kusuma, M. Manju, C. R. Ravikumar, V. G. Dileepkumar, A. Naveen Kumar, M. S. Santosh, H. C. Ananda Murthy and K. Gurushantha, *J. Nanomater.*, 2022, **13**, 3256611.